Materials Views
www.MaterialsViews.com

ADVANCED
ENERGY
MATERIALS
www.advenergymat.de

FULL PAPER

Ionic Reactivity at Contacts and Aging of Methylammonium Lead Triiodide Perovskite Solar Cells

*Jordi Carrillo, Antonio Guerrero, Sara Rahimnejad, Osbel Almora, Issac Zarazua, Elena Mas-Marza, Juan Bisquert, and Germà Garcia-Belmonte**

Hybrid lead halide perovskites have reached very large solar to electricity power conversion efficiencies, in some cases exceeding 20%. The most extensively used perovskite-based solar cell configuration comprises $CH_3NH_3PbI_3$ ($MAPbI_3$) in combination with electron (TiO_2) and hole 2,2′,7,7′-tetrakis(*N,N*-di-*p*-methoxyphenylamine)-9,9-*spiro*-bifluorene (*spiro*-OMeTAD) selective contacts. The recognition that the solar cell performance is heavily affected by time scale of the measurement and preconditioning procedures has raised many concerns about the stability of the device and reliability for long-time operation. Mechanisms at contacts originate observable current–voltage distortions. Two types of reactivity sources have been identified here: (i) weak Ti–I–Pb bonds that facilitate interfacial accommodation of moving iodine ions. This interaction produces a highly reversible capacitive current originated at the $TiO_2/MAPbI_3$ interface, and it does not alter steady-state photovoltaic features. (ii) An irreversible redox peak only observable after positive poling at slow scan rates. It corresponds to the chemical reaction between *spiro*-OMeTAD$^+$ and migrating I^- which progressively reduces the hole transporting material conductivity and deteriorates solar cell performance.

1. Introduction

Hybrid lead halide perovskites have reached very large solar to electricity power conversion efficiencies,[1–3] in some cases exceeding 20%.[4] In the last two years, a variety of configurations have been checked by modified cell structure, selective contacts, and perovskite materials utilized.[5–9] The most extensively used perovskite-based solar cell configuration comprises $CH_3NH_3PbI_3$ ($MAPbI_3$) or its analogous using chlorine precursor, $CH_3NH_3PbI_{3−x}Cl_x$, as absorber materials, in combination with electron (TiO_2) and hole 2,2′,7,7′-tetrakis(*N,N*-di-*p*-methoxyphenylamine)-9,9-*spiro*-bifluorene (*spiro*-OMeTAD) selective contacts. In spite of the spectacular advances in cell efficiency, many important aspects of the experimental observations on this system are not understood. Particularly intriguing is the hysteresis features in the response of the current density–voltage (*J*–*V*) curves[10–13] that have been related to a number of different explanations, as ferroelectric properties of the perovskite materials,[14–16] delayed electronic trapping processes,[17] or slow ion migration.[11,18,19] The recognition that the solar cell performance is heavily affected by time scale of the measurement and preconditioning procedures[9,17,20,21] has raised many concerns about the stability of the device and reliability for long-time operation.

It has been recognized that interfaces between the absorber perovskite and the contacting transport layers play a central role on the solar cell operation and performance.[22] Details of the interfaces surely depend on the synthetic methods used and materials processing. Interfacial electronic properties as energy level alignment constitute a relevant piece of knowledge that can be addressed through photoemission spectroscopies.[23,24] It is recognized that *spiro*-OMeTAD exhibits a nonoptimum energy level alignment at interfaces with perovskite absorbers, while the TiO_2 conduction band is in relatively fair energy alignment.[23] The use of other contact materials of diverse electronic character (either *n*- or *p*-type, and insulating) have revealed that the Fermi level within $MAPbI_3$ is strongly influenced by the substrate conductivity type.[24] Recent electrical measurements have shown that the potential drop concentrates near the $TiO_2/MAPbI_3$ contact forming a sort of *p*–*n* junction.[25,26] But interfaces evolve during solar cell operation, presumably by the presence of moving ions, in such a way that the connection between photoemission spectroscopy findings and the reported *J*–*V* distortions needs of complementary analysis.[27,28]

Dr. J. Carrillo, Dr. A. Guerrero, Dr. S. Rahimnejad,
O. Almora, Dr. I. Zarazua, Dr. E. Mas-Marza,
Prof. J. Bisquert, Prof. G. Garcia-Belmonte
Institute of Advanced Materials (INAM)
Universitat Jaume I
12071 Castelló, Spain
E-mail: garciag@uji.es
Dr. S. Rahimnejad
Department of Cemistry, Faculty of Science Yadegar-e-Imam Khomeini
(RAH) Shahre Rey Branch
Islamic Azad University
Tehran 18155-144, Iran
Prof. J. Bisquert
Department of Chemistry
Faculty of Science
King Abdulaziz University
Jeddah 21589, Saudi Arabia
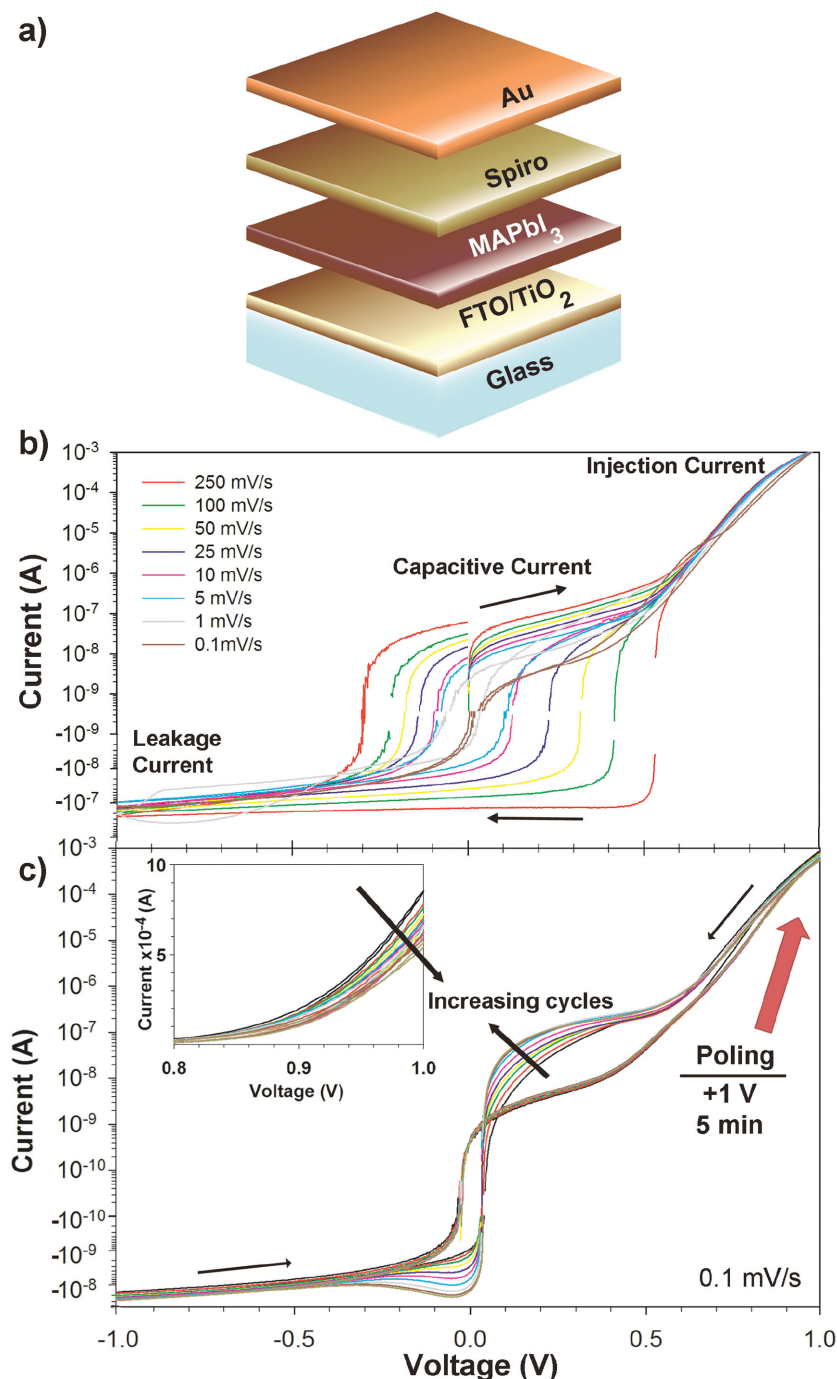
Figure 1. a) Structure of the planar solar cells. A thin MAPbI$_3$ layer (200 nm) is sandwiched between TiO$_2$ and *spiro*-OMeTAD selective contacts. b) Dark currents measured at different scan rates both for a positive and negative sweep. Three different mechanisms are identified as a function of the voltage, i.e., operation currents caused by carrier injection at V > 0.5 V, leakage currents observed at negative voltages (V < −0.5 V), and capacitive currents at −0.5 V < V < 0.5 V exhibiting dependence on the voltage scan rate. The slowest scan rate approaches a steady-state response. c) Cycled experiments including positive poling during 5 min. Positive scan (no poling) reproduces steady-state behavior. Negative scans induce incremental redox peaks after successive cycles. The process is only partially reversible. Inset: The injection current at forward bias decreases with cycling.

Here, we provide insights about time-dependent photovoltaic operation by discerning the locus of hysteresis response. We show that contact phenomena distort the *J–V* curve. Using different cell structures, we differentiate for the first time the different types of interactions of the standard electrode contacts. They display qualitatively different sources of reactivity at the interface between MAPbI$_3$ and the transporting layers. At TiO$_2$ contact we obtain reversible capacitive currents. On the other hand, irreversible ionic reaction occurs between mobile ions in MAPbI$_3$ and *spiro*-OMeTAD organic hole extracting layer. Only the latter irreversible behavior may cause significant long term aging by reduction of *spiro*-OMeTAD conductivity, and it is therefore a key point for engineering of the solar cell toward long time robust operation.

Recent experimental work shows a connection between capacitive current and hysteresis behavior in hybrid lead halide perovskites.[27] The microscopic phenomenon responsible for capacitive dark currents is the ionic electrode polarization, similar to double-layer capacitive effects, while the perovskite absorber layer behaves as a solid electrolyte able to interact with the contacting transport layers. However, it has not been determined which contact interface, either MAPbI$_3$/TiO$_2$, MAPbI$_3$/*spiro*-OMeTAD, or both, originates the observed capacitive response even in dark conditions. In this study, we report scans of current–voltage curves, both in solar cells of planar structure FTO (fluorine-doped tin oxide)/TiO$_2$/MAPbI$_3$/*spiro*-OMeTAD/Au (**Figure 1**a), and in planar perovskite layers with symmetric contacts of both types, electron and hole extracting electrodes. The purpose of the investigation is to differentiate which contact or part of the solar cell is causing specific hysteresis of irreversible features in current–voltage curves causing detrimental effects on the solar cell long time performance.

2. Results and Discussion

Figure 1b shows that capacitive currents dominate current–voltage response in the dark within the central voltage window. In addition, one observes injection currents at positive voltages (>0.5 V) and leakage currents at negative bias (< −0.5 V). Here the diode convention (common in Electronics)

www.MaterialsViews.com

ADVANCED
ENERGY
MATERIALS
www.advenergymat.de

FULL PAPER

is used: positive bias implies negative voltage at the cathode (ITO/TiO$_2$) contact, in such a way that electrons are injected through the cathode and holes through the anode (Au/*spiro*-OMeTAD). It is remarkable how the hysteresis disappears when approaching steady-state conditions, being highly reversible as the signal level is independent on the sweep direction.

Positive poling (1 V during 5 min) alters the quasi steady-state response (low scan rate) as observed in Figure 1c. However, cycled negative poling does not produce any effect on previous signals obtained for positive poling experiments (see Figure S1, Supporting Information). Figure 1c shows that a positive peak initially developed at ≈0.2–0.3 V is enlarged for successive poling cycles. This additional signal is only partially compensated by a negative peak appearing at ≈−0.1 – 0.0 V. In addition, injection current at forward bias is reduced upon cycling (inset of Figure 1c). We conclude that polarization and slow scan rates produce a partially reversible peak with an incremental effect indicating recurrent chemical interactions and forward current reduction at large bias. We note that this last behavior is different from the effect produced by bias preconditioning under illumination.[29] It causes a noncapacitive distortion of the current–voltage characteristics by ion-induced contact barrier modification.

Samples of symmetrical devices are useful to investigate separate electrode effects occurring in solar cells. As explained in the Experimental section, 500 µm-thick MAPbI$_3$ pellets are prepared and sandwiched between contact electrodes comprising transport layers (see Figures S2 and S3 (Supporting Information) for X-ray diffraction (XRD) and scanning electron microscopy (SEM) images). Symmetrical samples of structure FTO/TiO$_2$/MAPbI$_3$/TiO$_2$/FTO (**Figure 2**a) and Au/*spiro*-OMeTAD/MAPbI$_3$/*spiro*-OMeTAD/Au (**Figure 3**a) are prepared. Figure 2c shows the response when two TiO$_2$ contact layers are used. Perfect square-like signals clearly indicate the occurrence of capacitive currents comparable to those obtained for complete solar cells (0.1 µA for 250 mV s^{-1} scan rate) in Figure 1b. The fact that both solar cells and symmetrical devices yield similar current level, despite the huge difference in MAPbI$_3$ layer thickness (200 nm for thin films and 500 µm for pellets), corroborates the interfacial origin of the response. Figure 2d shows a linear dependence between current level and scan rate which allows extracting capacitive values approximately equal to 2 µF cm^{-2}, again in good agreement with typical double layer capacitors of order 10 µF cm^{-2}. It is also observed that polarization does
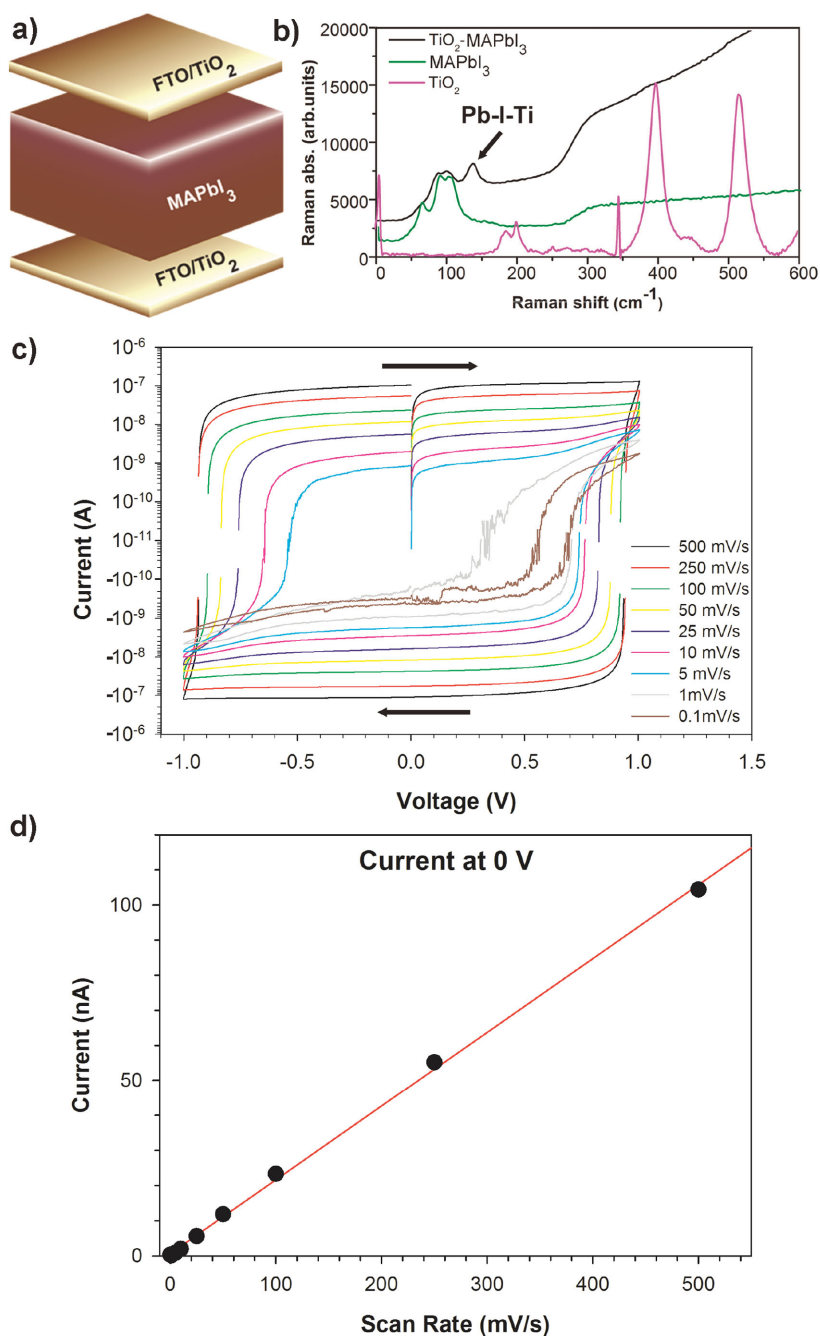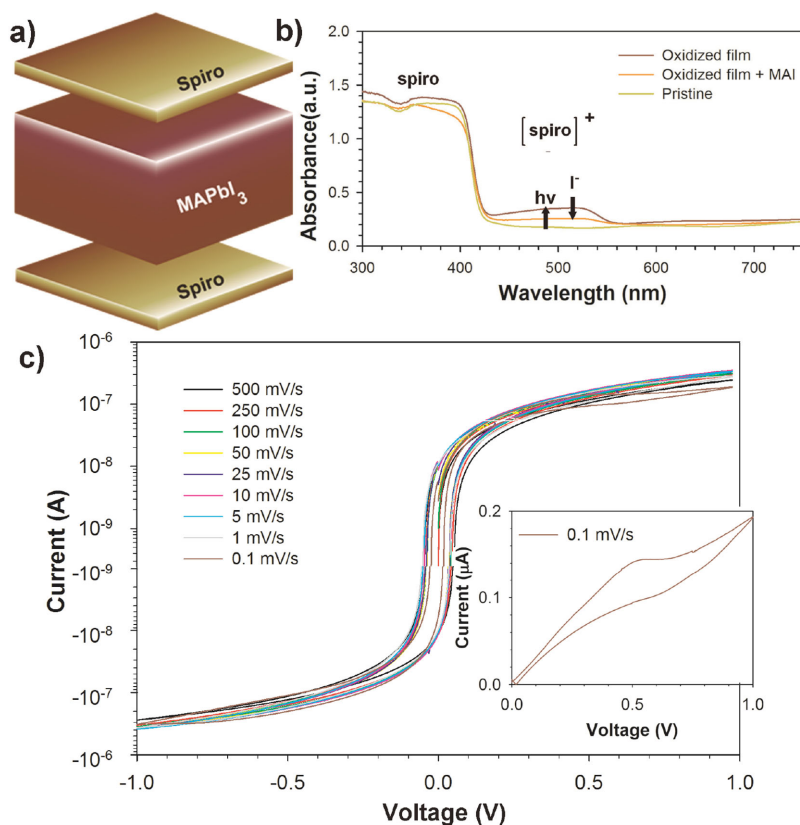

Figure 2. a) Structure of MAPbI$_3$ (500 µm) symmetric devices with TiO$_2$ contact layers. b) Raman spectra illustrating the formation of Ti–I–Pb bonds upon reaction between MAI and PbI$_2$. c) Capacitive currents exhibited by TiO$_2$/MAPbI$_3$/TiO$_2$ samples. Perfect square-like, scan rate-dependent responses are obtained indicating electrode capacitance behavior. d) Current level at 0 V as a function of the scan rate. The linear slope corresponds to ≈2 µF cm^{-2}.

not induce any additional feature in the form of redox peaks (Figure S4, Supporting Information). It is concluded that dark capacitive currents originate through electrode polarization at TiO$_2$/MAPbI$_3$ interfaces.

The *J–V* response changes completely when Au/*spiro*-OMeTAD/MAPbI$_3$/*spiro*-OMeTad/Au samples (Figure 3a) are analyzed. Figure 3c shows that only ohmic currents are

Figure 3. a) Structure of MAPbI$_3$ (500 μm) symmetric devices with *spiro*-OMeTAD contact layers. b) Absorption spectra of films of pristine and oxidized *spiro*-OMeTAD layers, and the reduction of the polaronic band (≈500 nm) by reaction with a source of I$^-$. c) Current–voltage characteristics of *spiro*-OMeTAD/MAPbI$_3$/*spiro*-OMeTaAD samples exhibiting ohmic, scan rate-independent behavior. At the slowest scan rate (inset) MAPbI$_3$ interacts with *spiro*-OMeTAD producing detectable signals. *spiro*-OMeTaAD is prepared without lithium salts to exclude Li$^+$ migration and de-doping.

observed. Because of the thick perovskite layer used it is expected that currents (presumably electronic leakage currents) are mainly governed by the bulk transport properties. In any case the response is observed to be scan-rate independent. In order to verify if additional signals are present, in similarity to redox peaks of Figure 1c, it is necessary to explore in detail low scan rate signals. The inset of Figure 3c shows in linear scale a current peak that slightly distorts the base ohmic behavior, only observable at 0.1 mV s^{-1} and also at negative bias. Therefore, analysis of symmetrical devices using hole-transporting layers suggests that MAPbI$_3$ interacts with *spiro*-OMeTAD producing detectable signals. *Spiro*-OMeTaAD is prepared without lithium salts to exclude Li$^+$ migration and de-doping. Results of *spiro*-OMeTaAD layers processed with lithium bis(trifluoromethylsulphonyl)imide are shown in Figure S5 (Supporting Information).

Our experiments have led us to separate two types of contact layer/perovskite interactions: either highly reversible one, producing the capacitive response originated at the TiO$_2$/MAPbI$_3$ interface, or in the form of a well-differentiated redox peak related to the *spiro*-OMeTAD/MAPbI$_3$ contact. Reversibility indicates a weak chemical interaction as those occurring in polarized surfaces forming an interface charge of adsorbed ions.

A computational study of the TiO$_2$/MAPbI$_3$ interface by De Angelis and co-workers,[30] indicates that TiO$_2$/perovskite interaction occurs mainly through the binding of perovskite iodine atoms to under-coordinated Ti(IV) atoms of the TiO$_2$ surface. Moreover, the two materials interact only weakly, as seen by the little hybridization found between the perovskite Pb *s–p* states and the Ti *d* orbitals constituting the TiO$_2$ conduction band. As a result an electrical dipole is formed with ≈4.8 D per nm^2 of TiO$_2$ surface. The identification of the TiO$_2$/MAPbI$_3$ chemical bonds along with evidences of easy iodine (defect) migration in perovskite-like materials[31,32] suggests a mechanism able to explain the observation of capacitive currents of Figures 1b and 2c by the reversible and facile interfacial ionic accommodation promoted by moving I$^-$.

The direct reaction between MAPbI$_3$ and commercially available TiO$_2$ nanoparticles has been investigated here to verify the formation of Ti–I–Pb bonds. The perovskite material has been synthesized by mixing methylammonium iodide (MAI) and PbI$_2$ (1:1) in dimethylformamide (DMF) followed by solvent evaporation (see the Experimental Section). By using Raman spectroscopy, Ti–I–Pb bonds are identified in the product (Figure 2b). Sign of hydrolysis is not observed as the characteristic band at 215 cm^{-1} for PbI$_2$ is not present.[33] When Raman spectra of the product are compared with reagents, a new band at 137 cm^{-1} appears which suggests evidence for Ti–I–Pb bond generation without the presence of an applied bias as in the case of devices. The observed capacitive current is then understood by means of the diagram shown in **Figure 4**. At positive applied bias iodide migrates toward the *spiro*-OMeTAD contact, a positive charge is generated at MAPbI$_3$ interface in close contact to the TiO$_2$ layer, and charge is compensated by the injection and accumulations of electrons at TiO$_2$. Finally, at negative bias I$^-$ is accumulated at MAPbI$_3$ layer contacting TiO$_2$. Ti–I–Pb bonds easily accommodate excess or defect ionic charge in a highly reversible way causing the capacitive currents.

A totally different scenario is observed at the *spiro*-OMeTAD/MAPbI$_3$ interfaces. *Spiro*-OMeTad requires partial oxidation in order to work efficiently as a hole extraction layer.[34] Indeed, photooxidation readily takes place under illumination with oxidized *spiro*-OMeTAD$^+$ concentrations observed above 10% during solar cell testing under ambient conditions. Partially oxidized *spiro*-OMeTAD molecules is known to increase hole conductivity of the layer.[35,36] Here, iodide migration and reaction with *spiro*-OMeTAD layer is monitored by absorption measurements (Figure 3b). A pristine *spiro*-OMeTAD film only shows a characteristic band between 300–420 nm. After oxidation in the presence of oxygen, the polaronic band corresponding to *spiro*-OMeTAD$^+$ at about 500 nm becomes evident. This polaronic species is stabilized by the presence of weakly coordinating

www.MaterialsViews.com

ADVANCED
ENERGY
MATERIALS
www.advenergymat.de

FULL PAPER

anions as those present in bis(trifluoromethyl) sulphonylimide (TFSI) to maintain electroneutrality. However, if the film is treated with a source of I⁻ ions, such as MAI, the intensity of the polaronic band decreases dramatically. This result is not surprising as iodide ions are highly coordinating. In order to rule out the effect of LiTFSI, similar experiments have been carried out in the absence of this additive (see Figure S6, Supporting Information). By reaction of *spiro*-OMeTAD in solution with oxidizing reagent containing a poorly nucleophilic anion ($NOBF_4$), the polaronic band appears at 500 nm, again confirming that the band corresponds to the *spiro*-OMeTAD polaron. Recovery of a neutral species with a higher extinction coefficient by further reaction with MAI is again observed. Overall, the chemical reaction can be expressed as in Equation (1)

$$spiro-OMeTAD^+ + I^- \rightarrow spiro-OMeTAD-I \qquad (1)$$
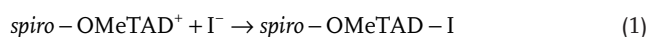
As discussed previously, the redox peak in Figure 1c enlarges after each positive poling cycle. One can then imagine a situation as sketched in Figure 4: At positive poling iodine ions migrate to the *spiro*-OMeTAD contact, and intercalate into the hole transport layer. This promotes reaction with previously oxidized *spiro*-OMeTAD molecules. By this way *spiro*-OMeTAD returns to its neutral state reducing the *p*-doped character of the hole contact layer. The reaction shown in Equation (1) occurs in a highly irreversible manner. This observation entails a progressive reduction in the conductive properties of the *spiro*-OMeTAD layer that finally produces a detrimental effect on the photovoltaic operation. This last mechanism agrees with the progressive reduction in the current at higher positive bias observed in the inset of Figure 1d. As the *spiro*-OMeTAD layer conductivity is reduced, the injection current is limited upon cycling.

3. Conclusion

In summary, two types of reactivity sources have been identified: (a) Weak Ti–I–Pb bonds facilitate interfacial accommodation of moving iodine ions. This interaction produces a highly reversible capacitive current originating at the TiO_2/MAPbI₃ interface. This mechanism does not alter the steady-state photovoltaic features. (b) An irreversible redox peak, only observable after positive poling at slow scan rates, corresponds to the chemical reaction between *spiro*-OMeTAD⁺ and migrating I⁻ which progressively reduces the hole transporting material conductivity and deteriorates the solar cell performance. We remark that during operation, a large photovoltage (≈1 V) is expected to occur for perovskite solar cells. A positive voltage causes ion movement and, as a consequence, aging effects through contact layer reaction. It is therefore essential to draw attention to chemical interactions between the absorber perovskite and the contact layers if this technology aims to reach long-term stability.
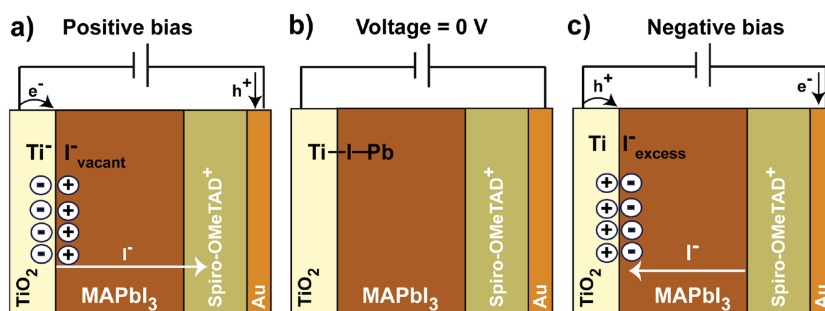
Figure 4. Diagram representing iodide migration and chemical species present at the interfaces. a) At positive-bias iodine ions are forced to migrate toward the hole selective contact where the reaction with *spiro*-OMeTAD⁺ occurs. The iodide defective layer is formed at the TiO_2/MAPbI₃ interface. b) At zero-bias the neutral case appears. c) At negative-bias *spiro*-OMeTAD only partially returns to its oxidized, conductive state. Iodide ions accumulate at the TiO_2/perovskite interface.

4. Experimental Section

Solar Cells—Substrate Preparation: FTO-coated glass substrates (25 mm × 25 mm, Pilkington TEC15, ≈15 Ω sq⁻¹ resistance) were etched with zinc powder and HCl (2 M) to obtain 0.224 cm² of active electrode area. The substrates were cleaned with soap (Hellmanex) and rinsed with MilliQ water and ethanol. Then, the sheets were sonicated for 15 min in a solution of acetone: isopropanol (1:1 v/v), rinsed with ethanol, and dried with compressed air. After that, a UV/ozone treatment was performed for 15 min. Then, a TiO_2 blocking layer was deposited onto the substrates by spray pyrolysis at 450 °C, using a titanium diisopropoxide bis(acetylacetonate) (75% in isopropanol, Sigma-Aldrich) solution diluted in ethanol (1:39, v/v), with oxygen as carrier gas. After the spraying process, the films were kept at 450 °C for 5 min.

Mesoporous TiO_2 Layer: When needed, a mesoporous TiO_2 layer was deposited by spin-coating at 4000 rpm during 60 s using a TiO_2 paste (Dyesol 18NRT, 20 nm average particle size) diluted in terpineol (1:3, weight ratio). After drying at 80 °C, the TiO_2 layers were heated at 450 °C for 30 min and cooled to room temperature. The thickness determined by scanning electron microscopy was ≈200 nm.

Perovskite Deposition: A total of 100 μL of the perovskite precursor solution (2.64 mmol of CH_3NH_3I and 0.88 mmol of $PbCl_2$ 1 mL of DMF) was spin-coated inside the glove box at 2000 rpm for 60 s. After the deposition, the substrate was kept at 100 °C for 10 min. Next, the substrates were heated at 100 °C during 1 h in an oven under air stream.

Hole Transport Layer Deposition (HTM): A 300–400 nm-thick HTM was deposited on top of the perovskite substrates by spin coating at 4000 rpm for 30 s under air conditions, using 100 μL of *spiro*-OMeTAD solution. The *spiro*-OMeTAD solution was prepared by dissolving 72.3 mg of (2,2′,7,7′-tetrakis(*N,N′*-di-*p*-methoxyphenylamine)-9,9′-*spiro*-bifluorene) and 28.8 μL of 4-*tert*-butylpyridine in 1 mL of chlorobenzene. When needed 17.5 μL of a stock solution of 520 mg mL⁻¹ of lithium bis(trifluoromethylsulphonyl)imide in acetonitrile was also added to the *spiro*-OMeTAD solution.

Gold Electrode Deposition: The deposition of 60 nm of gold was performed by thermal evaporation under ultrahigh vacuum conditions, using a commercial MBraun vacuum chamber. Before beginning the evaporation, the chamber was evacuated until pressure of 1 × 10⁻⁶ mbar.

Film Preparation—FTO/TiO_2 Compact Layer Films: A compact TiO_2 layer was deposited onto the cleaned substrates, by spray pyrolysis at 450 °C, using a titanium diisopropoxide bis(acetylacetonate) (75% in isopropanol, Sigma-Aldrich) solution diluted in ethanol (1:39, v/v), with oxygen as carrier gas. After the spraying process, the films were kept at 450 °C for 5 min. *FTO/Spiro-OMeTAD Films*: A 300–400 nm-thick of

HTM was deposited on top of the cleaned substrates by spin-coating, following the procedure previously explained.

CH$_3$NH$_3$PbI$_3$ Pellets: CH$_3$NH$_3$PbI$_3$ was synthesised by evaporation of DMF in a solution containing stoichiometric amounts of lead iodide (1.00 g, 1 eq) and methyl ammonium iodide (0.345 g, 1 eq). The mixture was placed in an open crystallization dish into a well-ventilated oven at 130 °C during 3 h, the mixture was stirred every 30 min. The black powder was characterized by XRD to confirm the pure perovskite crystallographic form (Figure S2, Supporting Information). Alternatively, SEM analysis shows the aspect of perovskite powder (Figure S3, Supporting Information). Films were prepared by pressing at 6 ton CH$_3$NH$_3$PbI$_3$ powder (0.25 g) into a 13 mm pellet die. Thicknesses of the pellets prepared in this manner range from 500–600 μm according to SEM data (Figure S3, Supporting Information).

Assembly of Symmetric Devices: Symmetric devices were prepared by placing a perovskite film between the outer contacts, either FTO/TiO$_2$ or FTO/ spiro-OMeTAD, and the sandwich structure was clamped to ensure a good electrical contact. The contacts were created using crocodile clips.

Solar Cells Characterization: The incident photon to current efficiency (IPCE) was performed using a Xenon lamp power source coupled with a monochromator controlled by a computer. Photocurrent was measured using an optical power meter 70310 from Oriel Instruments and a Si photodiode to calibrate the system. Current density–voltage (*J–V*) curves were performed under 1 sun illumination (100 mW cm^{-2}) using a Xenon arc lamp simulator (Sun 2000, ABET Technologies) with an AM 1.5 G spectral filter and a Keithley 2400, previously calibrated with an NREL Si solar cell (Figure S7, Supporting Information). All the measurements were performed with an opaque mask of 0.11 cm^2 and without encapsulation. The dark current–voltage and chronoamperometric curves were obtained by the use of a potentiostat/galvanostat (Autolab PGSTAT20). The initial potential was established at 0 V whereas the voltage ranged from 1 to −1 V. These experiments were carried out after the IPCE measurement and chronoamperometric experiments, in order to study their electrochemical behavior before and after the polarization of the solar cell. The chronoamperometric curves were performed applying a voltage of +1 V (or −1 V) during 5 and 15 min. The dark conditions were obtained by coating the solar cells completely with an aluminium foil. The optical absorption spectra of the active layers were recorded by a Cary 500 Scan VARIAN spectrophotometer in the 300–2000 nm range using an integrating sphere. Oxidized spiro-OMeTAD films were generated by keeping deposited film in the dark under ambient conditions over a period of one month. The film was treated with a solution of methyl ammonium iodide (5 mM) in isopropanol. The absorption band corresponding to oxidized spiro-OMeTAD reduces its intensity indicating that a source of nucleophilic atoms such as I$^-$ can react with oxidized spiro-OMeTAD to recover neutral species. For Raman experiments, the perovskite material has been synthesized by mixing MAI and PbI$_2$ (1:1) in DMF as solvent followed by solvent evaporation. Alternatively, the chemical reaction is carried out in ethanol, as poorly solubilizing solvent, with stirring at room temperature. Relatively high energy (80 mW) and very low excitation times (1 s) are used together with a holographic filter with a cutoff edge at 70 cm^{-1}. Raman spectroscopy measurements were carried out with a dispersive spectrometer NRS-3100 (Jasco).

Supporting Information

Supporting Information is available from the Wiley Online Library or from the author.

Acknowledgements

[1] N.-G. Park, *J. Phys. Chem. Lett.* **2013**, *4*, 2423.

[2] H. J. Snaith, *J. Phys. Chem. Lett.* **2013**, *4*, 3623.

[3] N. J. Jeon, J. H. Noh, Y. C. Kim, W. S. Yang, S. Ryu, S. I. Seok, *Nat. Mater.* **2014**, *13*, 897.

[4] M. A. Green, K. Emery, Y. Hishikawa, W. Warta, E. D. Dunlop, *Prog. Photovoltaics* **2015**, *23*, 1.

[5] K. Wojciechowski, S. D. Stranks, A. Abate, G. Sadoughi, A. Sadhanala, N. Kopidakis, G. Rumbles, C.-Z. Li, R. H. Friend, A. K.-Y. Jen, H. J. Snaith, *ACS Nano* **2014**, *8*, 12701.

[6] G. A. Sepalage, S. Meyer, A. Pascoe, A. D. Scully, F. Huang, U. Bach, Y.-B. Cheng, L. Spiccia, *Adv. Funct. Mater.* **2015**, *25*, 5650.

[7] X. Xu, Z. Liu, Z. Zuo, M. Zhang, Z. Zhao, Y. Shen, H. Zhou, Q. Chen, Y. Yang, M. Wang, *Nano Lett.* **2015**, *15*, 2402.

[8] O. Malinkiewicz, A. Yella, Y. H. Lee, G. M. Espallargas, M. Graetzel, M. K. Nazeeruddin, H. J. Bolink, *Nat. Photonics* **2014**, *8*, 128.

[9] T.-Y. Yang, G. Gregori, N. Pellet, M. Grätzel, J. Maier, *Angew. Chem.* **2015**, *127*, 8016.

[10] H. J. Snaith, A. Abate, J. M. Ball, G. E. Eperon, T. Leijtens, N. Kimberly, S. D. Stranks, J. T.-W. Wang, K. Wojciechowski, W. Zhang, N. K. Noel, *J. Phys. Chem. Lett.* **2014**, *5*, 1511.

[11] E. L. Unger, E. T. Hoke, C. D. Bailie, W. H. Nguyen, A. R. Bowring, T. Heumüller, M. G. Christoforod, M. D. McGehee, *Energy Environ. Sci.* **2014**, *7*, 3690.

[12] N. J. Jeon, J. H. Noh, Y. C. Kim, W. S. Yang, S. Ryu, S. I. Seok, *Nat. Mater.* **2014**, *13*, 897.

[13] R. S. Sanchez, V. Gonzalez-Pedro, J.-W. Lee, N.-G. Park, Y. S. Kang, I. Mora-Sero, J. Bisquert, *J. Phys. Chem. Lett.* **2014**, *5*, 2357.

[14] J. M. Frost, K. T. Butler, A. Walsh, *APL Mater.* **2014**, *2*, 081506.

[15] J. Wei, Y. Zhao, H. Li, G. Li, J. Pan, D. Xu, Q. Zhao, D. Yu, *J. Phys. Chem. Lett.* **2014**, *5*, 3937.

[16] H.-W. Chen, N. Sakai, M. Ikegami, T. Miyasaka, *J. Phys. Chem. Lett.* **2015**, *6*, 164.

[17] Y. Shao, Z. Xiao, C. Bi, Y. Yuan, J. Huang, *Nat. Commun.* **2014**, *5*, 5784.

[18] A. Dualeh, T. Moehl, N. Tétreault, J. Teuscher, P. Gao, M. K. Nazeeruddin, M. Grätzel, *ACS Nano* **2014**, *8*, 362.

[19] Z. Xiao, Y. Yuan, Y. Shao, Q. Wang, Q. Dong, C. Bi, P. Sharma, A. Gruverman, J. Huang, *Nat. Mater.* **2015**, *14*, 193.

[20] R. Gottesman, E. Haltzi, L. Gouda, S. Tirosh, Y. Bouhadana, A. Zaban, E. Mosconi, F. De Angelis, *J. Phys. Chem. Lett.* **2014**, *5*, 2662.

[21] E. J. Juárez-Pérez, R. S. Sánchez, L. Badia, G. Garcia-Belmonte, Y. S. Kang, I. Mora-Sero, J. Bisquert, *J. Phys. Chem. Lett.* **2014**, *5*, 2390.

[22] J. Berry, T. Buonassisi, D. A. Egger, G. Hodes, L. Kronik, Y.-L. Loo, I. Lubomirsky, S. R. Marder, Y. Mastai, J. S. Miller, D. B. Mitzi, Y. Paz, A. M. Rappe, I. Riess, B. Rybtchinski, O. Stafsudd, V. Stevanovic, M. F. Toney, D. Zitoun, A. Kahn, D. Ginley, D. Cahen, *Adv. Mater.* **2015**, *27*, 5102.

[23] P. Schulz, E. Edri, S. Kirmayer, G. Hodes, D. Cahen, A. Kahn, *Energy Environ. Sci.* **2014**, *7*, 1377.

[24] E. M. Miller, Y. Zhao, C. C. Mercado, S. K. Saha, J. M. Luther, K. Zhu, V. Stevanovic, C. L. Perkins, J. v. de Lagemaat, *Phys. Chem. Chem. Phys.* **2014**, *16*, 22122.

[25] A. Guerrero, E. J. Juarez-Perez, J. Bisquert, I. Mora-Sero, G. Garcia-Belmonte, *Appl. Phys. Lett.* **2014**, *105*, 133902.

[26] C.-S. Jiang, M. Yang, Y. Zhou, B. To, S. U. Nanayakkara, J. M. Luther, W. Zhou, J. J. Berry, J. v. de Lagemaat, N. P. Padture, K. Zhu, M. M. Al-Jassim, *Nat. Commun.* **2015**, *6*, 8397.

[27] O. Almora, I. Zarazua, E. Mas-Marza, I. Mora-Sero, J. Bisquert, G. Garcia-Belmonte, *J. Phys. Chem. Lett.* **2015**, *6*, 1645.

[28] H.-S. Kim, I.-H. Jang, N. Ahn, M. Choi, A. Guerrero, J. Bisquert, N.-G. Park, *J. Phys. Chem. Lett.* **2015**, *6*, 4633.

[29] W. Tress, N. Marinova, T. Moehl, S. M. Zakeeruddin, M. K. Nazeeruddin, M. Grätzel, *Energy Environ. Sci.* **2015**, *8*, 225.

[30] V. Roiati, E. Mosconi, A. Listorti, S. Colella, G. Gigli, F. De Angelis, *Nano Lett.* **2014**, *14*, 2168.

[31] J. M. Azpiroz, E. Mosconi, J. Bisquert, F. De Angelis, *Energy Environ. Sci.* **2015**, *8*, 2118.

[32] C. Eames, J. M. Frost, P. R. F. Barnes, B. C. O'Regan, A. Walsh, M. S. Islam, *Nat. Commun.* **2015**, *6*, 7497.

[33] M. Ledinský, P. Löper, B. Niesen, J. Holovský, S.-J. Moon, J.-H. Yum, S. De Wolf, A. Fejfar, C. Ballif, *J. Phys. Chem. Lett.* **2015**, *6*, 401.

[34] U. B. Cappel, T. Daeneke, U. Bach, *Nano Lett.* **2012**, *12*, 4925.

[35] W. H. Nguyen, C. D. Bailie, E. L. Unger, M. D. McGehee, *J. Am. Chem. Soc.* **2014**, *136*, 10996.

[36] L. Badia, E. Mas-Marzá, R. S. Sánchez, E. M. Barea, J. Bisquert, I. Mora-Seró, *APL Mater.* **2014**, *2*, 081507.